https://doi.org/10.5194/egusphere-2026-5452
Preprint. Discussion started: 25 September 2026

3-D characterization of Arctic lake ice with polarimetric SAR tomography at X- and C-band

Paloma Saporta[1,2], Matteo Pardini[1], Evan J. Wilcox[3], Julia Boike[4,5], and Irena Hajnsek[1,2]

[1]Microwaves and Radar Institute (HR), German Aerospace Center (DLR), Münchener Straße 20, 82234 Wessling, Germany
[2]Institute of Environmental Engineering (IFU), Swiss Federal Institute of Technology (ETH), Laura-Hezner-Weg 7, 8093 Zurich, Switzerland
[3]Department of Earth System Sciences, Earth and Society Research Hub (ESRAH), University of Hamburg, Allende-Platz 2, 20146 Hamburg, Germany
[4]Permafrost Research Section, Alfred Wegener Institute Helmholtz Centre for Polar and Marine Research, Telegrafenberg A45, 14473 Potsdam, Germany
[5]Geography Department, Humboldt-Universität zu Berlin, Unter den Linden 6, 10099 Berlin, Germany

Correspondence: Paloma Saporta (paloma.saporta@dlr.de)

Abstract. This study investigates for the first time the three-dimensional structure of Arctic lake ice based on tomographic reconstruction from a polarimetric, multi-baseline airborne Synthetic Aperture Radar (SAR) data set. The tomographic reconstruction indicates the presence of two strong interfaces at both X- and C-band, which can be attributed, based on field observations, to the air/ice and ice/liquid water interfaces. This means that the tomographic reconstruction is sensitive to the thickness of the ice layer of the investigated lakes. The reconstructed vertical reflectivity profiles are found to vary with polarization, therefore they can only be interpreted with a dedicated polarimetric analysis. In some lakes, we observe regions characterized by scattering with high entropy focused at the ice/water interface. We propose several hypotheses regarding the physical origin of these regions. Finally, requirements for the estimation of lake ice thickness from multi-baseline SAR are formulated to support the planning of future spaceborne SAR missions with tomographic capabilities.

1 Introduction

Lakes are ubiquitous in the Arctic, and lake ice cover is an important component of the cryosphere. Arctic lake ice is typically composed of congelation ice (also called “black ice”), which forms as ice crystals grow downward into the water while heat is exchanged between the water body and the atmosphere (Jeffries et al., 1994; Morris et al., 1995). The resulting ice layer can extend up to 2 m below the snow cover, and it can be "bedfast" if it extends until the lake bed, or "floating" if liquid water remains between the ice layer and the bed. Ice can be clear or contain gas bubbles that are typically tubular and elongated in the direction orthogonal to both the upper air/ice and the lower ice/water or ice/ground interfaces (Gow and Langston, 1977; Weeks et al., 1981). These bubbles have a diameter in the millimeter range (Gow and Langston, 1977; Jeffries et al., 1994) and are often located closer to the lower interface.

Monitoring Arctic lakes benefits from the use of active sensors such as Synthetic Aperture Radar (SAR), as observations can be carried out during polar night, nearly independently of weather conditions, and with high spatial and temporal resolutions.

https://doi.org/10.5194/egusphere-2026-5452
Preprint. Discussion started: 25 September 2026

The emitted radar pulses penetrate the snow cover and ice layer, interact with the physical elements in the snow/ice/water or snow/ice/ground system, and are backscattered to the radar. The received SAR signals therefore depend on 3-D structural and electromagnetic parameters like ice thickness, bubble content, surface roughness and dielectric contrasts at the interfaces. However, the understanding of how to parameterize polarimetric and interferometric SAR measurements in terms of lake ice structural and dielectric characteristics is at a rather early stage of development, essentially because of the lack of comprehensive SAR measurements and associated ground truth. As a consequence, the qualitative characterization of lake ice from SAR measurements, as well as parameterization, methodology and accuracy of quantitative inversions are constrained by a priori assumptions. The most common ones are about the nature of the dominant scattering contributions. For instance, in early airborne radar studies in the 1970's the strong backscatter observed over floating ice at X-band (Weeks et al., 1977) was associated to a large(r) dielectric contrast at the ice/water interface, and attributed to the presence of a double-bounce interaction between the ice/water interface and the tubular bubbles in the ice (Weeks et al., 1981). This motivated the use of backscatter intensity to determine the bedfast or floating nature of the lower ice interface. But later studies relying on fully polarimetric measurements at X-, C- and L-band related lake ice backscatter to a single-bounce mechanism at the ice/water interface (Atwood et al., 2015; Gunn et al., 2018). Its roughness was attributed to the presence of facets at the bottom of the ice volume or to the extrusion of bubble terminuses. The assumption of a dominant scattering contribution at the ice/water interface was used also in Wegmüller et al. (2010) to estimate ice thickness from C-band cross-track interferometric SAR (InSAR) measurements. For this, the InSAR phase of the shore was taken as a reference, and compensated from the phase measured within the lake. Recent differential SAR interferometry (D-InSAR) studies were based on a similar reasoning to relate the (temporal) interferometric phase to the change in ice thickness (Wakabayashi et al., 2019; Siles et al., 2022). In Yitayew et al. (2017a) the reconstruction of the 3-D SAR reflectivity (backscattered power) distribution of lake ice by means of tomographic SAR (TomoSAR) techniques was a critical step allowing the detection and separation of scattering contributions in height without a priori assumptions. By means of a high-resolution ground-based experiment, it became clear that at C- and X-band scattering contributions from interfaces at different heights (e.g. air/snow, snow/ice, interfaces within the ice, ice/water) can actually equally contribute to the total received signal. However, the experiment was performed only on a limited area within the lake and in one polarization.

In this context, the objective of this study is to make a further step into the 3-D characterization of Arctic lake ice by exploring and analyzing a new SAR data set, acquired during the PermASAR campaign of the German Aerospace Center (DLR) in the West Canadian Arctic in 2019. This data set provides a unique chance to fill the gaps of previous studies in terms of dimensionality, type and coverage of the available SAR measurements. The fully polarimetric multi-baseline acquisition configuration enables not only a polarimetric tomographic (Pol-TomoSAR) model-free separation of scattering contributions in height, but also their characterization. At the same time, the high resolution and larger ground coverage allows one to characterize the spatial variability within and across lakes. To the extent of the authors' knowledge, this is the first Pol-TomoSAR attempt to the 3-D characterization of lake ice from airborne data. The rest of the article is structured as follows. Section 2 describes the polarimetric tomographic algorithm used to reconstruct polarimetric parameters (including the reflectivity) as a function of height. The chosen algorithm can increase the vertical resolution of the reconstruction with limited polarimetric distortions. The airborne SAR data set and field measurements are described in Sect. 3, and the expected tomographic per-

https://doi.org/10.5194/egusphere-2026-5452
Preprint. Discussion started: 25 September 2026

formance is discussed. Section 4 describes the obtained Pol-TomoSAR reconstructions over different lakes, which are further discussed in Sect. 5. Hypotheses on the physical origins of particular polarimetric features are made and addressed as well. The implications for future missions with tomographic capabilities are presented in Sect. 6. Finally, Sect. 7 summarizes findings and draws the conclusions of the entire study.

2 Methods: Pol-TomoSAR

TomoSAR is an established technique to reconstruct the 3-D reflectivity of vertically extended media, related to the 3-D distribution of scatterers (Reigber and Moreira, 2000). A tomographic stack is composed of M Single Look Complex (SLC) images acquired from different tracks or orbits separated by spatial baselines (displacements). Each baseline has a component in the line-of-sight direction (i.e., the parallel baseline $B_{\|}$), and in the across-range direction (i.e., the perpendicular baseline $B_{\perp}$). The interferometric phase difference of a pair of acquisitions is related to the corresponding height change through the associated vertical wavenumber. For a monostatic system and propagation in air, the vertical wavenumber is expressed as:

$$k_z = \frac{4\pi}{\lambda}\frac{\Delta\theta}{\sin(\theta)} \qquad (1)$$

where λ is the radar wavelength, θ the local incidence angle, $\Delta\theta$ the incidence angle difference of the pair induced by $B_{\perp}$, and z the vertical height.

The quality of a tomographic reconstruction depends critically on the number and spatial distribution of tracks or orbits. The resulting distribution of k_z values determines two important parameters: the Rayleigh resolution limit in height δ_z, which relates to the ability to resolve different scatterers, and the height of ambiguity ΔH_z, which defines the height interval in which an ambiguity-free reconstruction can be obtained (Reigber and Moreira, 2000). The Rayleigh resolution limit in height depends on the vertical wavenumber k_z^{large} associated with the largest perpendicular baseline, and is given by:

$$\delta_z = \frac{2\pi}{k_z^{large}}. \qquad (2)$$

The usable largest baseline (hence the achievable Rayleigh resolution limit) is limited by the so-called critical baseline (Zebker and Villasenor, 1992). At the critical baseline the phase contributions of scatterers within the same resolution cell are very different. As a consequence, the two acquisitions become uncorrelated (Moreira et al., 2013), and they do not contribute to the TomoSAR reconstruction.

In contrast, the height of ambiguity depends on the vertical wavenumber k_z^{small} associated with the smallest perpendicular baseline, and is given by:

$$\Delta H_z = \frac{2\pi}{k_z^{small}}. \qquad (3)$$

δ_z and ΔH_z are critical parameters to be compared to the physical extent of the scattering volume. The achievable resolution in height from usual TomoSAR acquisitions ranges from even less than 1 m (Joerg et al., 2018) to several meters (Cazcarra-Bes et al., 2022), and the height of ambiguity typically ranges from several meters (Joerg et al., 2018) to several tens of meters (Cazcarra-Bes et al., 2022).

https://doi.org/10.5194/egusphere-2026-5452
Preprint. Discussion started: 25 September 2026

All single-polarization TomoSAR algorithms reconstruct (real-valued) power profiles only. Different algorithms can achieve different radiometric accuracies and resolutions in height in the order of or even better than the Rayleigh limit. The final choice depends in general on the application requirements. Pol-TomoSAR extends TomoSAR reconstructions by including polarimetric data. In this way, scattering contributions at different heights can be separated and characterized in terms of backscattered power and phase for different polarization combinations (Sauer et al., 2011; Ferro-Famil et al., 2012). In particular, full-rank extensions (Ferro-Famil et al., 2012) allow the reconstruction of a polarimetric covariance matrix $\mathbf{C}(z)$ as a function of height z.

This article relies on a novel reconstruction algorithm introduced in Vecchia et al. (2026) improving the radiometric accuracy of the Pol-TomoSAR Capon technique originally introduced in Ferro-Famil et al. (2012). This algorithm exploits a linear relationship between the real and imaginary parts of complex polarimetric covariances in the lexicographic basis (HH, VV, HV) and the backscattered power at certain transformed polarizations, as shown in Hoekman and Vissers (2003). The Pol-TomoSAR reconstruction is based on the $3M \times 3M$-dimensional polarimetric covariance matrix $\mathbf{R_p} = E(\boldsymbol{y} \cdot \boldsymbol{y}^H)$ at each range-azimuth cell where E is the expectation operator and H the Hermitian (transpose and complex conjugate) operator. $\boldsymbol{y}$ is the polarimetric scattering vector defined as $\boldsymbol{y} = [\boldsymbol{y_1}^H, \boldsymbol{y_2}^H, \boldsymbol{y_3}^H]^H$, and each $\boldsymbol{y_i}$ for $i = 1,...,3$ collects the M SLC complex amplitudes at the i-th polarization. First, the tomographic covariance matrix $\mathbf{R_k}$ of each $k = 1,...,9$ transformed polarization is obtained from $\mathbf{R_p}$ as:

$$\mathbf{R_k} = (\boldsymbol{w_k} \otimes \mathbf{I_M})^H \mathbf{R_p} (\boldsymbol{w_k} \otimes \mathbf{I_M}). \tag{4}$$

In Eq. (4), $\otimes$ is the Kronecker product and $\mathbf{I_M}$ is the identity matrix of order M. The vectors $\boldsymbol{w_k}$ are defined in Table I of Vecchia et al. (2026). Then, a single-polarization Capon power reconstruction is performed at each height z, for each transformed polarization k:

$$P_k(z, \boldsymbol{w_k}) = \boldsymbol{h}^H(z) \mathbf{R_k} \boldsymbol{h}(z) \tag{5}$$

with

$$\boldsymbol{h}(z) = \frac{\mathbf{R_{kL}}^{-1} \boldsymbol{a}(z)}{\boldsymbol{a}^H(z) \mathbf{R_{kL}}^{-1} \boldsymbol{a}(z)}. \tag{6}$$

In Eq. (6), $\boldsymbol{a}(z)$ is the so-called M-dimensional steering vector with m-th element $a_m(z) = e^{jk_{z,m}z}$. $\mathbf{R_{kL}}$ is the diagonally loaded covariance matrix in the k-th transformed polarization defined as $\mathbf{R_{kL}} = \mathbf{R_k} + \delta \bar{P}_k \mathbf{I_M}$ where $\bar{P}_k$ is the mean backscattered total power at that polarization and δ is the loading factor, set to $\delta = 0.5$. The reconstructed powers at each height and for each transformed polarization are collected in the vector $\boldsymbol{p}(z)$ such that $(\boldsymbol{p}(z))_k = P_k(z, \boldsymbol{w_k})$. Finally, the reconstructed powers are recombined at each height to retrieve polarimetric covariances in the original lexicographic basis. To this end, the real and imaginary parts of the elements of the polarimetric covariance matrix are obtained in the vector $\boldsymbol{c}(z)$ as:

$$\boldsymbol{c}(z) = \mathbf{B} \boldsymbol{p}(z) \tag{7}$$

https://doi.org/10.5194/egusphere-2026-5452
Preprint. Discussion started: 25 September 2026

with the elements of $\boldsymbol{c}(z)$ defined in Table I of Vecchia et al. (2026) and the matrix $\mathbf{B}$ defined in Hoekman and Vissers (2003). At each height z, the final polarimetric covariance matrix $\mathbf{C}(z)$ in the lexicographic basis is reconstructed from the elements of $\boldsymbol{c}(z)$.

While the lexicographic basis is relevant from a radar-system point of view, as this is the polarization basis of most operating airborne and spaceborne systems, the Pauli basis is suited to describe scattering mechanisms. The backscattered power in the Pauli 1 polarization ($HH+VV$) is maximized for scattering with an odd number of bounces (e.g. surface scattering), in the Pauli 2 polarization ($HH-VV$) is maximized for scattering with an even number of bounces (e.g. dihedral or double-bounce scattering), and the Pauli 3 polarization ($2HV$) is generally associated with scattering from a volume of particles. As a consequence, to ease the interpretation of the reconstructed polarimetry of the separated scattering contributions, the polarimetric covariance matrices $\mathbf{C}(z)$ reconstructed in the lexicographic basis are transformed into polarimetric coherency matrices $\mathbf{T}(z)$ in the Pauli basis by means of a standard polarization basis change (Cloude, 2009). The conventional TomoSAR power reconstructions are extracted from the diagonal elements of $\mathbf{T}(z)$.

Once the polarimetric coherency matrices $\mathbf{T}(z)$ are reconstructed, standard polarimetric methodologies can be used to characterize scattering contributions. Here we apply a polarimetric Cloude-Pottier entropy / alpha decomposition (H/α) (Cloude and Pottier, 1997) based on the eigenvalue / eigenvector decomposition of $\mathbf{T}(z)$. This decomposition can be used to identify the simultaneous occurrence of multiple contributions with different scattering matrices within a resolution cell. The entropy ranges between 0 and 1, and measures the randomness of the backscattering process, or equivalently the number of effective scattering mechanisms in which $\mathbf{T}(z)$ can be decomposed. An entropy close to 0 indicates the presence of a (non-depolarizing) dominant scattering mechanism. As the entropy increases from 0, more scattering mechanisms occur simultaneously, until the limit case of entropy close to 1. In this case, $\mathbf{T}(z)$ is dominated by a (completely depolarized) random noise scattering process. α is related to the type of scattering mechanism. Typically, low α values (close to $0\,°$) indicate scattering from a surface (odd number of bounces), and high α values (close to $90\,°$) indicate a double-bounce interaction. Intermediate values indicate a dipole-like scattering behavior.

3 Data

The study lakes are situated near Trail Valley Creek (TVC, 68.7 °N, 133.5 °W), located in the Western Canadian Arctic. The TVC watershed is a well-studied continuous permafrost site characterized by gently rolling hills with shrub-tundra vegetation (Grünberg et al., 2020). The region encompasses several thermokarst lakes whose hydrological behavior has been studied in particular by Wilcox et al. (2022) and Wilcox et al. (2023). These lakes are typically a few meters deep, reach a maximum ice thickness of 1 m and are typically ice-covered from October to June (Wilcox et al., 2022; Wilcox, 2025b). Most lakes range between hundreds of meters to a few kilometers in breadth. Lakes that are deeper than 1 m tend not to fully freeze through in the winter, resulting in unfrozen sediments beneath them despite the surrounding permafrost terrain. Extensive methane bubbles have not been observed at these lakes, but thin tubular gas bubbles are likely present in the ice. The lakes were segmented

https://doi.org/10.5194/egusphere-2026-5452
Preprint. Discussion started: 25 September 2026

Table 1. Field measurements collected at the study lakes on the 26th of April 2019: ice thickness, snow thickness and ice regime.

Name	Lake 1	Lake 2	Lake 3	Lake 4	Lake 5
Ice thickness	1.05 m	1.05 m	1.0 m	0.95 m	1.10 m
Snow thickness	10 cm	10 cm	10 cm	15 cm	13 cm
Ice regime	floating	floating	floating	floating	floating

from the land and vegetation using the high-resolution vegetation classification map of Grünberg and Boike (2019) that was enhanced as described in Saporta et al. (2025).

3.1 Field measurements

Field measurements of ice thickness and ice regime were collected on the 26th of April 2019 (Wilcox, 2025a). At the center of each sampled lake, a hole was augered through the lake ice to measure its thickness; the thickness of the overlying snow and lake depth were also recorded. The measured ice thickness and snow thickness over the lakes selected for this study are shown on Table 1. The measured ice thickness is about 1 m, and it is expected to be uniform at each lake. All lakes had a floating ice regime (i.e., the ice was not frozen to the lake bed). Bedfast conditions are possible at the lake shores due to the reduced depth with respect to the center.

3.2 Airborne SAR data set

This study relies on data acquired during the Permafrost Airborne SAR Experiment campaign (PermASAR) carried out by the German Aerospace Center in 2019. The campaign aimed at improving the knowledge of the interaction between radar waves and the elements of permafrost landscapes (soil, vegetation, snow, ice). DLR's experimental airborne sensor F-SAR acquired data sets over 10 test sites along a North-South gradient in Canada. Flights were performed with different configurations (from interferometric to tomographic), and acquisitions were made at different frequencies (X-, C-, S- and L-band). Additional data analysis relying on the PermASAR campaign can be found in Saporta et al. (2025).

The data set over the TVC was acquired on the 23rd of March 2019, in a period where the lakes are frozen and the ice cover is well established, around one month before the field measurements. The acquisitions are fully polarimetric, and have sub-meter spatial resolution in both azimuth and range directions. The tomographic stack consists of $M = 8$ SLC images acquired in repeat-pass mode within two hours, allowing to neglect potential temporal decorrelation caused by wind-induced snow redistribution. The flown tracks were displaced in the horizontal direction to realize the required perpendicular baselines. All relevant system and acquisition parameters are reported in Table 2. It is worth noting that the Rayleigh resolution at L-band is coarse compared to the expected ice thickness. For this reason, the rest of this study focuses on X- and C-band.

The TomoSAR data set was processed and calibrated by means of the standard F-SAR repeat-pass interferometric processing chain including SLC focusing, calibration, co-registration, terrain phase compensation, and TomoSAR phase calibration (Reigber et al., 2013). A C-band polarimetric SLC composite of the study site for the reference acquisition is shown in Fig. 1,

https://doi.org/10.5194/egusphere-2026-5452
Preprint. Discussion started: 25 September 2026

Table 2. Summary of system and acquisition parameters of the DLR's F-SAR acquisitions over Trail Valley Creek, 23rd of March 2019, PermASAR campaign.

Frequency band	L	C	X
Wavelength, cm	22.6	5.7	3.1
Resolution [range, azimuth], m	[1.3, 0.6]	[1.0, 0.5]	[1.0, 0.5]
[Min., max.] incidence angle, deg		[25, 60]	
Horizontal track displacements[a], m		0, 5, 10, 15, 20, 30, 40, 100	
[Min., max.] κ_z at mid range[b], rad/m	[0.05, 0.8]	[0.2, 3.2]	[0.4, 5.8]
δ_z at mid range, m	8.0	2.0	1.1
ΔH_z at mid range, m	131	32	32

[a]The reference acquisition is the first acquisition of the stack.

[b]The reported minimum κ_z was obtained as an average of the κ_z of all the interferometric pairs with a 5 m horizontal track displacement, which was further averaged over the azimuth cells of the transect at mid range. The reported maximum κ_z was obtained from the interferometric pair with the largest baseline, and averaged over the azimuth cells of the transect at mid range. The values of δ_z and ΔH_z in the two following lines are obtained from the maximum and minimum κ_z values reported in the Table, respectively, and according to Eq. (2) and Eq. (3).

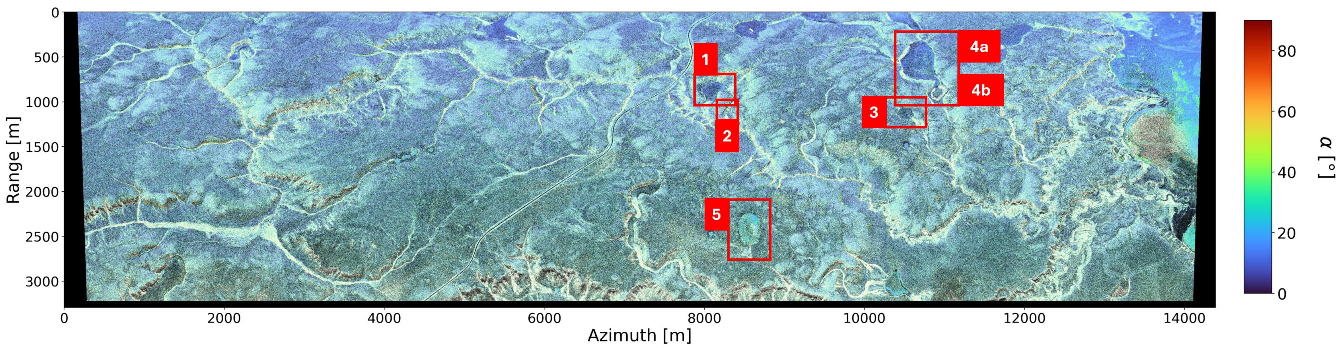

Figure 1. HSV representation of F-SAR acquisition over the Trail Valley Creek study site at C-band in radar geometry (azimuth, slant range). In the representation, the hue (H) corresponds to the polarimetric α angle, the saturation (S) is set to $s = 1 - H$ where H is the polarimetric entropy, and the value (V) corresponds to the total scattering power. Lakes are identified by their number; the red line delimits their extent.

and subsets over the investigated lakes are shown in Fig. 2. To increase interpretability, a Hue-Saturation-Value (HSV) representation has been chosen: the Hue (color) is the polarimetric α angle, the Saturation is set to $s = 1 - H$, and the Value is the total backscattering power. This combination allows at the same time to display both polarimetric indicators (α angle and entropy H) and to preserve the information of the backscattering power. In the study site, tall vegetation, typically around streams, appear as bright high-entropy features, while the short vegetation on hills appears as low-to-mid entropy, corresponding mostly to surface scattering (Saporta et al., 2025). The lakes appear in blue, suggesting low-entropy surface scattering. However, high-entropy regions can be recognized within certain lakes.

https://doi.org/10.5194/egusphere-2026-5452
Preprint. Discussion started: 25 September 2026

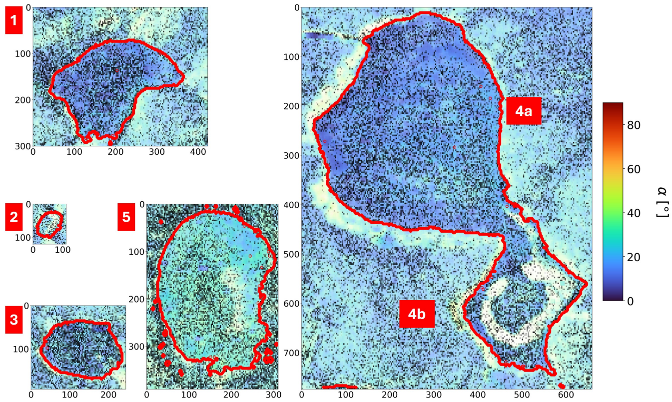

Figure 2. Subsets of Fig. 1 over the investigated lakes.

3.3 Selection of study lakes and expected tomographic performance

This study focuses on the five lakes where field measurements were taken in the same winter as the F-SAR campaign. The lakes are numbered from 1 to 5. Their locations are shown in Fig. 1 and Fig. 2, and the Rayleigh resolution limits at X- and C-band are reported in Table 3. Lakes 1 to 4 are located in the watershed of Trail Valley Creek, i.e., at mid-range of the SAR coverage, with medium incidence angle ranging from $35\,°$ to $42\,°$. Lake 5 is located more towards far range with an incidence angle of $54\,°$. For propagation in air, using Eq. (2), the Rayleigh resolution limit for Lakes 1 to 4 ranges from 0.6 m to 0.8 m at X-band, and from 1 m to 1.5 m at C-band. For Lake 5 the Rayleigh resolution becomes worse and reaches 1.5 m at X-band and even 2.7 m at C-band.

The evaluation of the expected TomoSAR performance at the five lakes should actually take into account the propagation of the radar waves in ice after refraction at the air/ice interface. Two effects must be considered, namely (i) the reduction of the propagation velocity as a consequence of the increase of the medium density, and (ii) the change of the propagation direction according to Snell's law. Accordingly, the vertical wavenumber becomes (Dall, 2007):

$$\kappa_{z,vol} = \kappa_z \frac{\epsilon_{ice}\cos(\theta)}{\sqrt{\epsilon_{ice} - \sin^2(\theta)}} \tag{8}$$

where ϵ_{ice} is the relative permittivity of ice. As a consequence, to account for the propagation in ice the Rayleigh resolution limit, Eq. (2) should be calculated using $\kappa_{z,vol}$ instead of κ_z. Compared to the second and third lines, the last two lines of Table 3 show the change of Rayleigh resolution for $\epsilon_{ice} = 3.2$, typical of freshwater ice. The effective increase of the largest vertical wavenumber induces a decrease of the Rayleigh resolution limit for all the selected lakes. The obtained values for Lakes 1 to 4 are below the measured ice thickness, hence allowing a reliable TomoSAR separation. The Rayleigh resolution limits for Lake 5 are still sub-optimal, especially at C-band.

https://doi.org/10.5194/egusphere-2026-5452
Preprint. Discussion started: 25 September 2026

Table 3. Incidence angle and Rayleigh resolution limit in height at the lakes under study.

Name	Lake 1	Lake 2	Lake 3	Lake 4a	Lake 4b	Lake 5
Incidence angle	39 °	42 °	42 °	35 °	40 °	54 °
Rayleigh resolution limit in height at X-band (air)	0.7 m	0.8 m	0.8 m	0.6 m	0.7 m	1.5 m
Rayleigh resolution limit in height at C-band (air)	1.3 m	1.5 m	1.5 m	1.0 m	1.3 m	2.7 m
Rayleigh resolution limit in height at X-band (ice)	0.5 m	0.6 m	0.6 m	0.4 m	0.5 m	1.3 m
Rayleigh resolution limit in height at C-band (ice)	0.9 m	1.0 m	1.1 m	0.7 m	0.9 m	2.3 m

4 Results

In this section, Pol-TomoSAR reconstruction results obtained with the algorithm presented in Sect. 2 are presented. As usual, the expectation operator E in the definition of $[R_P]$ has been implemented as an average of neighboring samples within multilook cells measuring 5 m $\times$ 5 m in the slant range and azimuth directions, and equivalent to 58 independent looks at both X- and C-band. The corresponding Pol-TomoSAR reconstructions have therefore the same resolution.

Before the tomographic processing, at each lake an additional local compensation of residual topographic and phase calibration errors was applied. To this end, first each lake was separated into range blocks where the residual error was assumed to be constant. For each block, an additional area at the lake shore was taken as reference, and only pixels with bare ground or short vegetation were selected according to the high-resolution vegetation classification map described in Sect. 3. Then, the phase difference of each SLC with respect to the reference one was averaged spatially over the selected pixels of each block. Finally, for each block, the resulting mean phases were compensated from each SLC before forming the multi-baseline covariance matrix.

Values of κ_z calculated in air have been used. On the one hand the hypothesis of a single homogeneous ice layer may not be verified, and on the other hand the corresponding permittivity cannot be guessed a priori. Therefore, appropriate values of $\kappa_{z,vol}$ can not be obtained.

4.1 Reconstructed power profiles in the Pauli basis

The Capon power reconstructions in the Pauli basis at X- and C-band are shown in Fig. 3 and Fig. 4, respectively, for a transect along azimuth in the center of the lakes and for the same locations on ground. Reconstructions of total backscattered power are shown on the last row of Fig. 3 and Fig. 4. They have been calculated as the sum of the power reconstructions in the three Pauli polarizations. All reconstructions are normalized at each azimuth pixel with respect to the corresponding maximum of the total power reconstructions in order to compare the relative power level of different polarizations. Concerning the total power reconstructions, it is worth remarking that the local normalization enhances the identification of the most powerful contributions, but it does not preserve backscatter power variations along the transect.

https://doi.org/10.5194/egusphere-2026-5452
Preprint. Discussion started: 25 September 2026

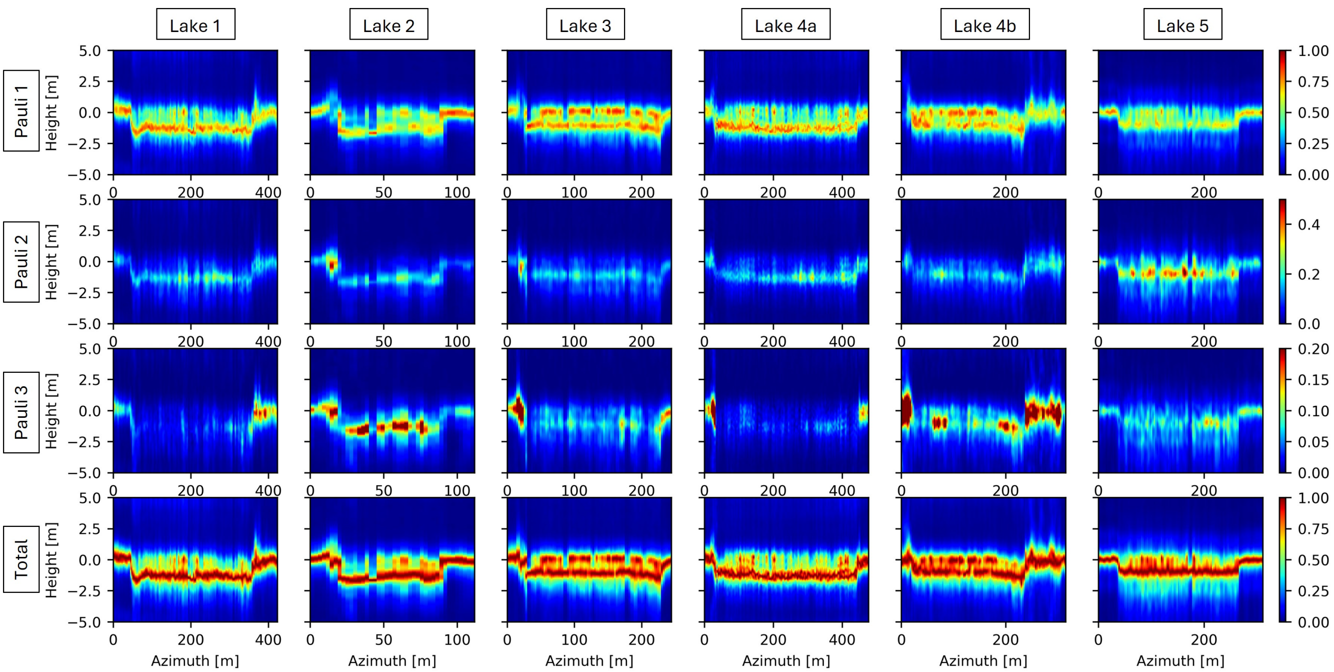

Figure 3. Capon Pol-TomoSAR power reconstructions along azimuth transects at the study lakes, X-band. The transects are in the Pauli polarizations: the first row corresponds to Pauli 1 ($HH+VV$), the second row to Pauli 2 ($HH-VV$), the third row to Pauli 3 ($2HV$) and the last row to the total power. Each column corresponds to a different lake, from Lake 1 to Lake 5. Each profile is normalized to the maximum total power at each azimuth bin.

In Fig. 3 and Fig. 4 lake shores are visible at both extremities of the transect. They are located around zero height as they have been used as a reference for the additional phase calibration. The lake pixels are located between the shores, and constitute the largest part of the transects. Reconstructions in different polarizations and lakes clearly show the presence of powerful peaks (local maxima) with height differences in the order of the ice thickness. This result confirms the expected tomographic performance. At Lake 5 and especially at C-band, the separation capability is reduced in accordance with the calculated resolution limit, that is the coarsest for that lake and in this configuration ($\delta_z = 2.7$ m in air in Table 3).

Relative weight of the scattering contributions: At both X- and C-band, the total power is dominated by the contribution of the Pauli 1 polarization (surface scattering). For most lakes, the Pauli 2 and Pauli 3 polarizations are the secondary contributions in this order. At C-band the relative contribution of Pauli 2 and Pauli 3 to the total power is weaker than at X-band. In certain lake sections there is a strong power contribution in the Pauli 3 polarization (Lake 2, Lake 4b), that is also associated with an increase in the Pauli 2 polarization by comparison with the other locations from the same lake.

Location and interpretation of the scattering contributions: Peaks of reconstructed profiles represent in general strong backscattering contributions. In the case of lake ice, their physical interpretation is attempted here, supported by previous studies in the literature (Yitayew et al., 2017a; Gunn et al., 2018). From Fig. 3 and Fig. 4 it is apparent that typically two peaks

https://doi.org/10.5194/egusphere-2026-5452
Preprint. Discussion started: 25 September 2026

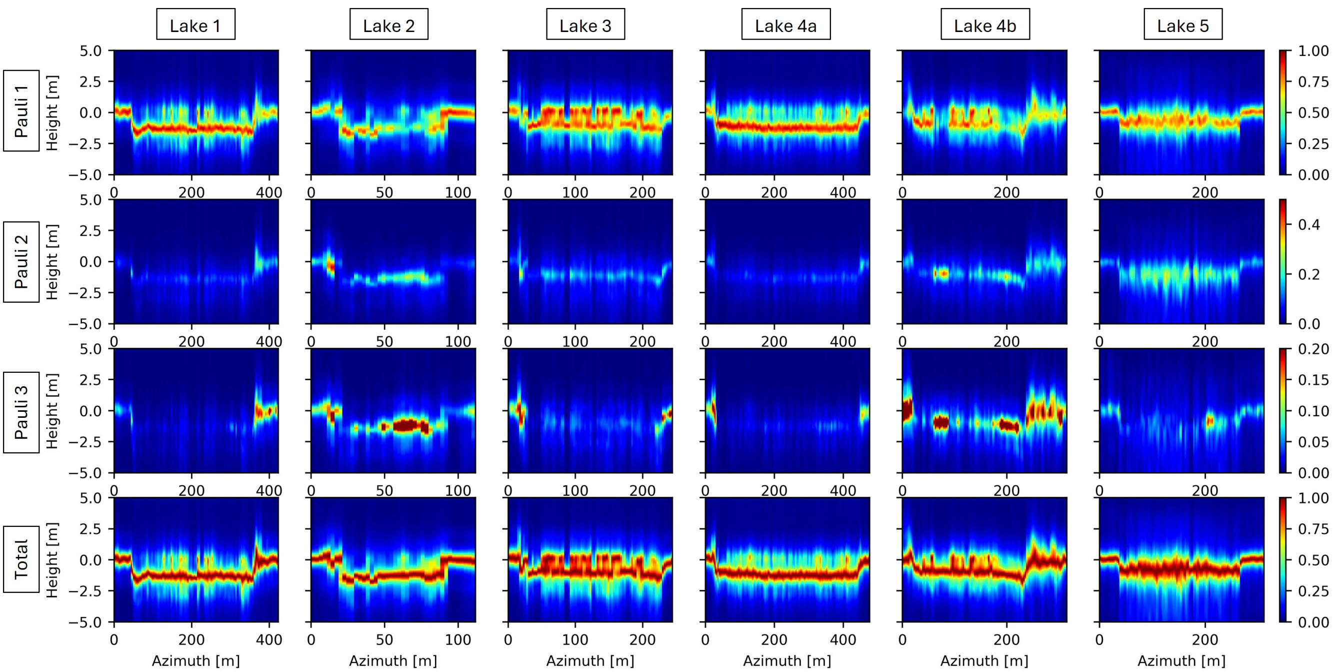

Figure 4. Capon Pol-TomoSAR power reconstructions along azimuth transects at the study lakes, C-band. The transects are in the Pauli polarizations: the first row corresponds to Pauli 1 ($HH+VV$), the second row to Pauli 2 ($HH-VV$), the third row to Pauli 3 ($2HV$) and the last row to the total power. Each column corresponds to a different lake, from Lake 1 to Lake 5. Each profile is normalized to the maximum total power at each azimuth bin.

are separated per reconstructed profile with quite spatially homogeneous locations. One peak is typically located close to the shore height (0 m), hence it is reasonable to relate it to the upper air/ice interface. The second peak is located below the first one at a height difference ranging from 0.6 m to 1 m (after approximately taking into account the ice dielectrics, as discussed in Sect. 3.3), corresponding to the expected ice thickness. The second peak therefore likely represents the lower ice/water interface. The association of the profile peaks to the interfaces can be further supported by the fact that at each interface a dielectric contrast occurs (between air and ice at the top and between ice and water at the bottom), which is expected to generate a very localized scattering contribution.

The total power profiles show some variability among the lakes. For all lakes, the strongest scattering contribution of the total power reconstructions comes from the lower interface. This is particularly true at C-band, despite the fact that the separation between two distinct interfaces is less clear than at X-band. This is certainly an effect of the lower resolution in height at C-band. However, a physical effect deriving from a weaker interaction of the incoming electromagnetic wave with the upper air/ice interface can not be excluded.

Some lakes display a contribution from the upper interface (Lake 3, Lake 4b) as well, or possibly from the ice volume (Lake 1, Lake 3, Lake 4a, Lake 5). Reconstructions in Pauli 1 indicate a clear contribution for most lakes from both upper and

https://doi.org/10.5194/egusphere-2026-5452
Preprint. Discussion started: 25 September 2026

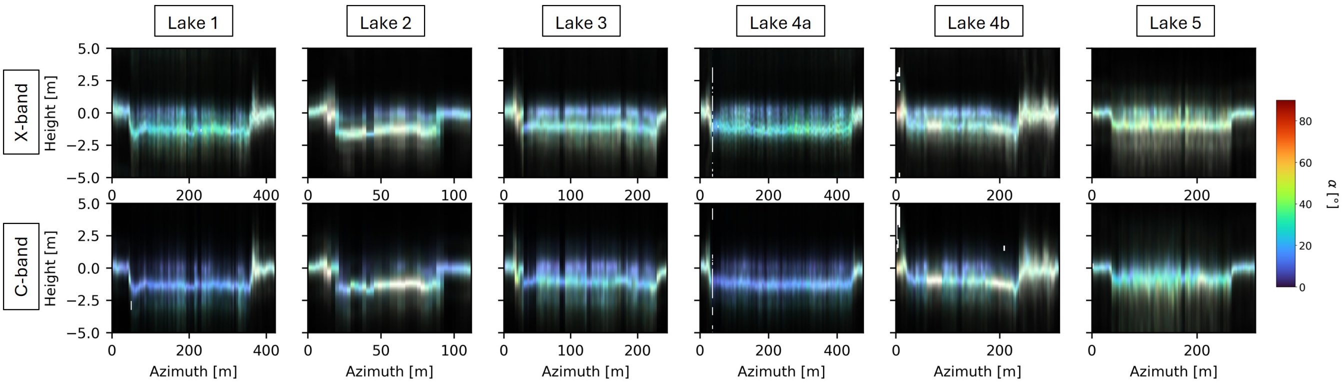

Figure 5. HSV representation at X-band (top row) and C-band (bottom row) obtained from the Capon Pol-TomoSAR reconstruction of the polarimetric covariance matrices along height. At each height, the hue (H) corresponds to the polarimetric α angle, the saturation (S) is set to $s = 1 - H$ where H is the entropy, and the value (V) is the total power reconstructed at that height, normalized to the maximum (see bottom rows of Fig. 3 and Fig. 4). Each column corresponds to a different lake, similarly to the previous figures.

lower interfaces. In Pauli 2, the contribution for all lakes is focused at the lower interface. Though the contribution in Pauli 3 is much weaker compared to the other polarizations, it is interesting to note that it is focused at the expected lower interface (see for instance Lake 2 and 4b at both X- and C-band, and for the other lakes in Fig. A1 and Fig. A2). Regarding the fact that the Pauli 2 and Pauli 3 contributions are focused at the lower interface, several explanations can be hypothesized, e.g. the occurrence of scattering at/close to the interface, or the occurrence of multiple scattering appearing focused at the interface. This is further discussed in Sect. 5.1.

4.2 Polarimetric scattering contributions

To investigate the type of the occurring scattering mechanisms, the Cloude-Pottier H/α decomposition has been applied to the polarimetric covariance matrix at each height of each transect location. To enhance visualization and interpretation, we use again a HSV representation as described in Sect. 3.2. In this manner, only cells with a dominant (non-depolarizing) scattering mechanism appear in color, and the color corresponds to the type of scattering mechanism as indicated by the α angle. Cells dominated by a (completely depolarized) random noise appear white. The HSV representations for the previous azimuth transects are shown for X-band and C-band in Fig. 5.

In the transects of Fig. 5 the shore appears white for some lakes, indicating complex scattering mechanisms from the vegetation and the ground. For other lakes the shore appears blue, indicating that surface scattering is the dominant contribution. Within the lake volume, at X-band the two interfaces already individuated in total power reconstructions of Fig. 3 are clearly visible in this representation as well. Most lakes display a strong lower interface with medium α angle, while the upper interface is associated with lower α values. In contrast, at C-band the lower interface shows low α values. In Lake 3 and Lake 4b, the upper interface also exhibit low α values. Interestingly, those lake sections of Lake 2 and Lake 4b that were noticed to be

https://doi.org/10.5194/egusphere-2026-5452
Preprint. Discussion started: 25 September 2026

associated with stronger relative power contributions in Pauli 2 and Pauli 3 at the lower interface are displayed in white in this representation, i.e., H close to 1 . It is interesting to note that this polarimetric analysis highlights the differences between the scattering occurring at X-band and C-band, which is consistent with the relative strength of the power reconstructions at single polarization.

The same HSV representation can be used to create lake sections at different heights, so as to retrieve indications on the spatial homogeneity of scattering for a whole lake extent. Sections at the heights of the lower and upper interfaces are shown in Fig. 7 for Lake 1, in Fig. 8 for Lake 3 and in Fig. 9 for Lake 4b. For each lake, the heights of lower and upper interfaces are extracted from a mean profile obtained by averaging reconstructions of the total backscattered power of Fig. 3 and Fig. 4 over the whole lake extent. The mean profiles are shown in Fig. 6 for all the lakes. Two peaks can be clearly distinguished in the X-band mean profiles, and their locations are assigned to the interface heights. The C-band mean profiles have typically a clear peak at the lower interface, but only an inflection at a height that is consistent with the upper interface at X-band and close to 0 m height. Therefore, at C-band, the location of the clear peak is assigned to the lower interface, and the height of 0 m is empirically assigned to the upper interface.

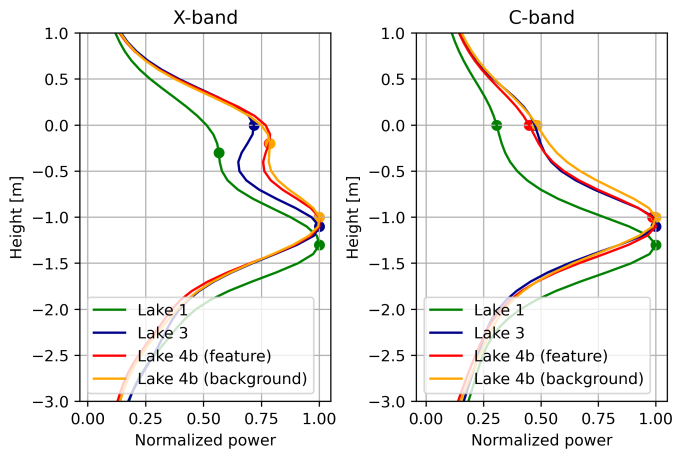

Figure 6. Mean profiles obtained by averaging reconstructions of the total backscattered power for the entire extent of Lakes 1, 3 and 4b. The dots indicate the extracted positions of the upper and lower interfaces.

In Fig. 7, Fig. 8 and Fig. 9, for both X-band and C-band, the lake surroundings appear bright at the height of the upper interface, which corresponds approximately to the peak of the shore reference. In Fig. 7 and Fig. 8, Lakes 1 and 3 appear spatially homogeneous at both frequencies, though some local patterns can be observed, e.g. at the lower interface of Lake 1 at X-band. Compared to Lake 1, Lake 3 exhibits more complex scattering at the lower interface at C-band. In Fig. 9, the high-entropy regions of the transects at the lower interface of Lake 4b in the transects of Fig. 5 appear spatially extended in the well-defined shape of a ring. The rest of the lake behaves similarly to Lake 1 and Lake 3.

The mean values of H and α averaged over the whole lake at both upper and lower interfaces are shown in Fig. 10 for X-band and Fig. 11 for C-band. For the Lake 4b, all the pixels with $H > 0.75$ at the lower interface were attributed to the the

https://doi.org/10.5194/egusphere-2026-5452
Preprint. Discussion started: 25 September 2026

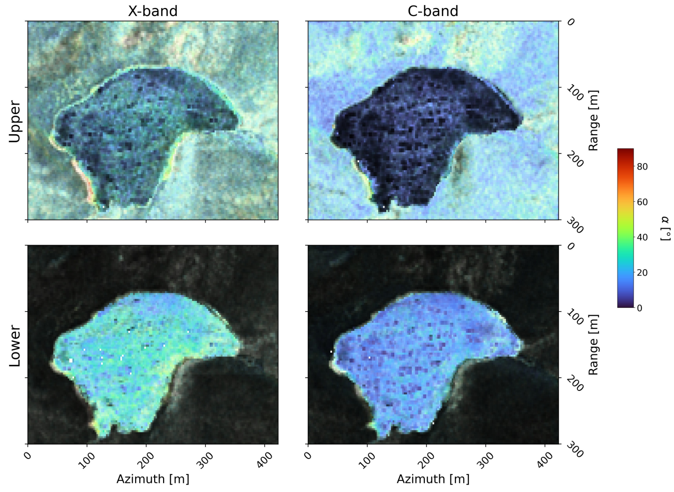

Figure 7. HSV representations at X- (left) and C-band (right) of Lake 1 in the range-azimuth plane at the upper (top) and lower (bottom) interfaces. The color scale corresponds to degrees.

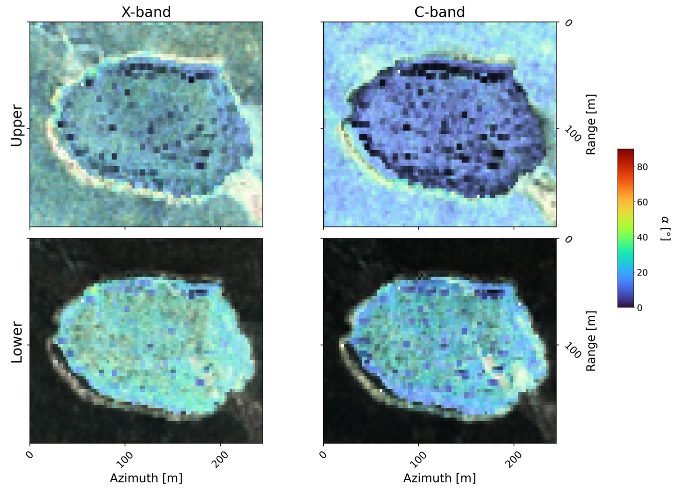

Figure 8. HSV representations at X- (left) and C-band (right) of Lake 3 in the range-azimuth plane at the upper (top) and lower (bottom) interfaces. The color scale corresponds to degrees.

https://doi.org/10.5194/egusphere-2026-5452
Preprint. Discussion started: 25 September 2026

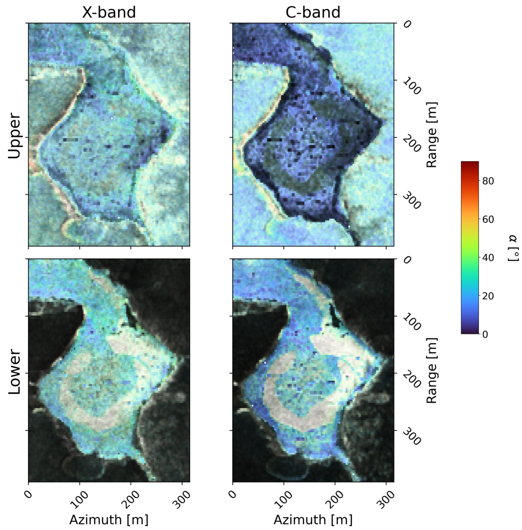

Figure 9. HSV representations at X- (left) and C-band (right) of Lake 4b in the range-azimuth plane at the upper (top) and lower (bottom) interfaces. The color scale corresponds to degrees.

high-entropy region and separated from the lake background. Lake 1, Lake 3 and the background of Lake 4b are characterized by smaller H and α values at C-band compared to X-band, and smaller H and α values at the upper interface compared to the lower interface. The high-entropy region also exhibits a larger H for the lower interface compared to the upper interface, however the entropy at the lower interface is larger at C-band than at X-band. It is important to note that for high entropy the α angle is constrained to a limited range of achievable values, and does not correspond directly to a certain type of scattering mechanism (Cloude and Pottier, 1997).

5 Discussion

In this section, the 3-D polarimetric signature of the lakes is discussed, with a particular attention to the high-entropy regions. Specific effects of the propagation of the signal within the ice are analyzed, and our results are compared with the previous ground-based TomoSAR studies.

5.1 3-D Polarimetric signature

The Pol-TomoSAR reconstructions confirm the previous widely accepted fact that at both X- and C-band backscattering contributions at the ice interfaces are significantly stronger than contributions within the ice volume. However, they also show that at C-band backscattering at the ice/water interface is not the only contribution to the total backscattered signal as assumed in Jeffries et al. (1994); Atwood et al. (2015); Gunn et al. (2018), but the air/ice interface can be significant as well.

https://doi.org/10.5194/egusphere-2026-5452
Preprint. Discussion started: 25 September 2026

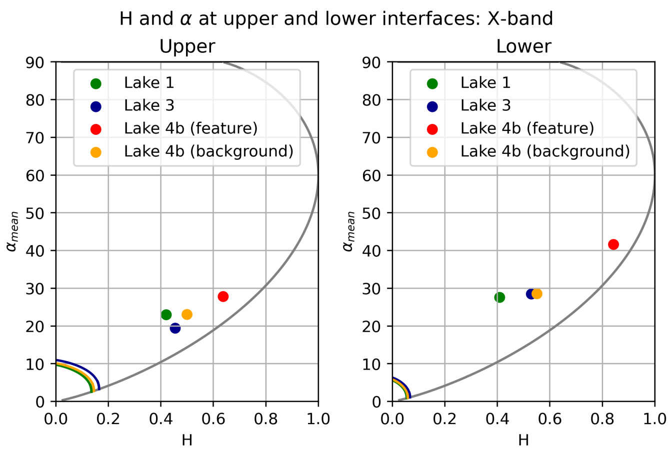

Figure 10. Location of several lakes in the H/α plane at X-band. Each point is a spatial average over the lake pixels, respectively at the upper (left) and lower (right) interfaces. The gray lines on each plot delimit the achievable H/α values. The colored lines correspond to the achievable values of H/α derived from the X-Bragg model at the incidence angle of the respective lake and for respectively an air/ice interface (left) and an ice/water interface (right). The change in propagation direction due to the refraction at the air/ice interface is accounted for. For each line, the width of the distribution of surface slope angles varies from 0 to π rad in the X-Bragg model.

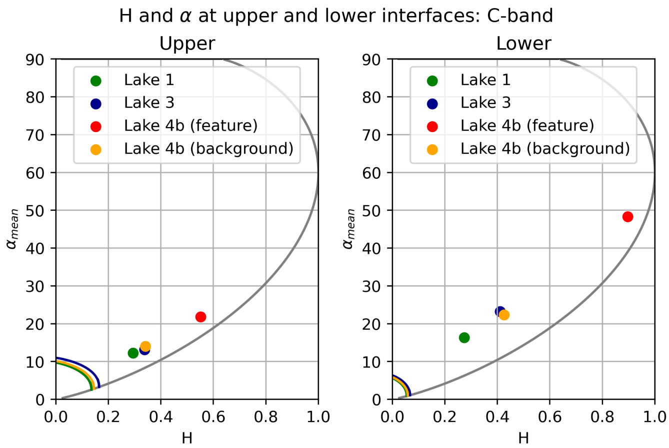

Figure 11. Location of several lakes in the H/α plane at C-band. Each point is a spatial average over the lake pixels, respectively at the upper (left) and lower (right) interfaces. The other elements of this figure are the same as in Fig. 10.

https://doi.org/10.5194/egusphere-2026-5452
Preprint. Discussion started: 25 September 2026

The H and α values obtained at each interface have been compared with the expected values provided by the extended Bragg (X-Bragg) model. It is commonly used to describe the polarimetric behavior of natural rough surfaces (Hajnsek et al., 2003), and was also proposed in the context of lake ice in Al-Kahachi (2014). Based on this model, a polarimetric coherency matrix and the associated H and α values are calculated as a function of the local incidence angle, the dielectric constants of the surface and of the medium in which the wave propagates, and the width of the distribution of surface slope angles, which accounts for surface roughness. The distribution width varies from 0 to π rad. On both Fig. 10 and Fig. 11, the modeled H/α values for an air/ice interface and an ice/water interface are compared to the Pol-TomoSAR H/α values at the upper and lower interfaces, respectively. As the incidence angles for Lakes 1, 3 and 4b are similar, the achievable H/α values for a rough surface modeled by X-Bragg are nearly coincident.

At the air/ice interface with $\epsilon_{air} = 1.0$ and $\epsilon_{ice} = 3.2$, and at the incidence angle in correspondence of the lakes, the X-Bragg models predicts $H < 0.16$ and $\alpha < 11\,°$ (Fig. 10 and Fig. 11, left side). At X-band, and to a lesser extent at C-band, the Pol-TomoSAR values are larger, which suggests that additional depolarizing effects are occurring. At these frequencies and especially at X-band, it is reasonable to hypothesize the presence of an additional volume scattering contribution induced by the thin snow cover above the lake ice.

At the ice/water interface, the initialization of the X-Bragg model requires to account for the refraction at the previous air/ice interface. Since the permittivity in ice is larger than the one in air, the refracted angle in ice is smaller than the incidence angle in air. In the X-Bragg model, steeper angles are associated with lower H/α values. This decrease counteracts the increase of H/α due to a larger dielectric contrast at the ice/water interface. Altogether, considering $\epsilon_{ice} = 3.2$ and $\epsilon_{water} = 80$, the X-Bragg model eventually predicts $H < 0.06$ and $\alpha < 6\,°$ (Fig. 10 and Fig. 11, right side). The Pol-TomoSAR values at the lower interface are well above this range at both X- and C-band. This suggests that surface scattering is not the only scattering mechanism at this interface. However, the interpretation of polarimetric observables at the ice/water interface is complicated by the occurrence of ambiguities owing to scattering mechanisms that are specific to the lake ice case. In particular, the presence of bubbles in the ice can lead to volume scattering (Al-Kahachi, 2014). Further, multiple scattering can also occur in the form of dihedral backscattering when the incoming wave is specularly reflected at the ice/water interface onto the volume and finally to the sensor (or inversely). Each scattering mechanism separately and their combination can lead to non-zero Pauli 2 and Pauli 3 contributions, which lead to similar H/α values as the Pol-TomoSAR ones (Al-Kahachi, 2014). These values depend on the shape (spheres to dipoles), orientation (random to oriented) and distribution of the cloud of particles, and these parameters have not been measured on the study site. In our case, volume scattering could be explained by the presence of a volume of gas bubbles in the lower part of the ice layer, with a scattering phase center height located close to the ice/water interface (distance in the order of the resolution in height). On the other hand, a volume of gas bubbles distributed at different heights can lead to higher entropy scattering via the dihedral backscattering of the cloud of particles. Therefore, one cannot conclude unequivocally on the types of scattering mechanism occurring at the ice/water interface, but one can definitely exclude the occurrence of solely rough surface scattering.

https://doi.org/10.5194/egusphere-2026-5452
Preprint. Discussion started: 25 September 2026

5.2 Presence of high-entropy regions

The Pol-TomoSAR analysis shows the presence of high-entropy regions associated with an increased relative power contribution in Pauli 2 and Pauli 3 polarizations. This is most striking on Lake 4b. Though the presence of these regions can already be observed from the SLC in Fig. 1, the Pol-TomoSAR analysis locates them at the ice/water interface. Interestingly, they appear only in certain lakes, and have sharp boundaries.

Unfortunately, the absence of ice cores at the time of the campaign does not allow a direct interpretation of the physical origin of these regions. However, we verified that they appear in Sentinel-2 optical imagery during freeze-up (visible on 1st of October 2018), and can be distinguished at break-up (visible on 31st of May 2019). At freeze-up, the regions appear darker than the surrounding snow-covered ice. This could suggest that either snow on the ice has been infiltrated with water, or that the ice is forming at a different time than at the rest of the lake. At break-up, the regions also appear darker than the surrounding ice. Based on these observations, several processes could cause the observed regions, alone or in conjunction:

- The first possible origin of these highly entropic regions is the presence of a refrozen snow layer, the so-called "snow-ice". Snow ice typically forms from flooding and subsequent freezing of a snow layer on top of a pre-existent ice layer, hence it consists in a sub-layer that is located at the top of the congelation ice. Since very similar dark regions are present in the Sentinel-2 optical imagery at the time of freeze-up, we consider this explanation to be the most likely. In previous studies, strong HV contributions have been related with the presence of snow-ice as a volume of scatterers (van der Sanden et al., 2012). In our case, the direct volume scattering from a potential snow-ice layer is excluded as this contribution would be focused at the upper interface and not at the lower interface as observed. However, a snow-ice volume could lead to other effects such as dihedral backscattering, with the incoming wave being reflected at the ice/water interface and subsequently scattered back to the radar by the particles of the snow-ice layer. Therefore, the presence of snow-ice correlating with an unusual polarimetric response is a possibility.

- Another explanation would be the spatial variability of the characteristics of gas bubbles in the congelation ice, such as shape and orientation, that would lead to a larger entropy compared to the rest of the lake. For instance, Al-Kahachi (2014) shows that both in the cases of dihedral and volume backscattering from a cloud of ellipsoids, the highest entropy is achieved for a cloud of randomly oriented dipoles. However, the presence of the regions already during freeze-up contradicts this hypothesis, since bubbles in the ice form throughout the season.

- Another possible explanation is the presence of randomly oriented facets at the ice/water interface. These facets have been observed in Yitayew et al. (2017b) and were associated with the increased scattering in HV. In our case, the fact that the regions appear during ice formation contradicts this hypothesis too.

- A final possible explanation could be a difference in ice crystal structure. Earlier studies such as Michel and Ramseier (1971); Gow (1986) show that two types of congelation ice can develop, depending on the meteorological conditions at the moment of the first ice formation. The two types are S1 type (granulated congelation ice), where the ice crystals grow with a vertical c-axis orientation, and S2 type (candled ice), where the ice crystals grow with a horizontal c-axis

https://doi.org/10.5194/egusphere-2026-5452
Preprint. Discussion started: 25 September 2026

orientation (Gow, 1986; Hobbs, 2010). If the candle ice structures of S2 ice act as oriented dihedral scatterers, this could explain the regions by attributing them to S2 ice type while the rest of the lakes would be S1 granulated congelation ice. The high entropy would then be due to the addition of the scattering mechanism to the ones already occurring in the ice and at the interfaces. This hypothesis is consistent with the observations from optical imagery, as different freezing time of the ice can be associated with different meteorological states, which in turn condition the type of primary ice.

5.3 Evidence for multiple-bounce

A few reconstructed power profiles (see e.g. Lake 3 in Fig. 3 and Fig. 4) exhibit a "tail" below the ice/water interface, still with a non-negligible backscattered power. Due to the absence of scatterers located physically below the ice/water interface, this tail could rather indicate multiple-bounce scattering between the ice/water interface and the ice/air interface, as the associated time delay leads to an apparently deeper scattering contribution. The symmetry suggests a ray path as follows: specular reflection at the ice/water interface, followed by backscatter at the ice/air interface, followed by reflection at the ice/water interface back to the radar. This phenomenon is mostly observed at C-band and only for certain lakes. It is important to remark that while this effect might have an influence on polarimetric observables in the general (non-tomographic) case as it contributes to the total signal, in the tomographic case the longer travel path leads to multi-bounces being focused below the ice/water interface, thereby not affecting the sections at upper heights and in particular the physical ice interfaces.

5.4 Comparison with ground-based TomoSAR results

It is interesting to compare the results of the high resolution ground-based TomoSAR experiment of Yitayew et al. (2017b) and Yitayew et al. (2017a) with the results of the current study. In the TomoSAR reconstruction over freshwater sea-ice of Yitayew et al. (2017b), three interfaces are visible at X-band: the air/snow, snow/ice and ice/seawater interfaces. It is to be noted that with the ground-based setup, resolution in the height direction of 14 cm could be achieved, for an on-site layer of 24 cm of dry snow above 28 cm thick sea ice. In our case, the air/snow and snow/ice interfaces can not be separated at X-band, due to the coarser spatial resolution in height compared to the snow layer, which was measured to be of 10 cm: only a single air/ice interface, that potentially includes the snow layer, can be detected from the Pol-TomoSAR reconstructions. Further on, Yitayew et al. (2017a) realized a similar set-up than Yitayew et al. (2017b) over lake ice and found that at both X- and C-band, the backscattering from surface and interface structures dominate the volume contributions. This has been observed also in this study. Finally, Yitayew et al. (2017b) noted that the snow/ice interface is the strongest backscattering contribution at X-band and VV polarization. In our case, at X-band, the main contribution in terms of total power consistently comes from the ice/water interface for most lakes, with a comparable contribution of the upper interfaces for some lakes. However, as shown in the Appendix, the main contribution in VV polarization comes alternatively from the upper (Lakes 3 and 5), the lower interface (Lakes 1 and 4) or both (Lakes 2 and 6), in relation with the occurring scattering mechanisms.

https://doi.org/10.5194/egusphere-2026-5452
Preprint. Discussion started: 25 September 2026

6 Implications for future missions with tomographic capabilities

The current results can be used to discuss requirements for a spaceborne mission to provide measurements suitable to obtain model-free TomoSAR reconstructions, e.g. for mapping ice thickness. In a multi-baseline case, it is necessary to assess which vertical wavenumber configuration is needed to allow at least the detection and localization of two interfaces. Usually, for spaceborne implementations a small number of baselines is preferred, as it either reduces the system complexity (case of a single-pass system), or the total revisit time (case of a repeat-pass system). Here, we focus on the minimum requirements that need to be satisfied.

From Eq (2), requiring a height resolution in ice better than $\delta_{z,ice}^{max}$ poses a requirement on the minimum value of the largest vertical wavenumber in ice $\kappa_{z,vol}^{large}$:

$$\frac{2\pi}{\kappa_{z,vol}^{large}} < \delta_{z,ice}^{max} \Rightarrow \kappa_{z,vol}^{large} > \frac{2\pi}{\delta_{z,ice}^{max}}. \tag{9}$$

Remembering from Eq. (8) that $\kappa_{z,vol}^{large} = a\kappa_z^{large}$ with $a = \frac{\epsilon_{ice}\cos(\theta)}{\sqrt{\epsilon_{ice} - \sin^2(\theta)}}$, a requirement on the largest vertical wavenumber κ_z^{large} follows as:

$$\kappa_z^{large} > \frac{1}{a}\frac{2\pi}{\delta_{z,ice}^{max}}. \tag{10}$$

Similarly, a requirement on the minimum height of ambiguity $\Delta H_{z,ice}^{min}$ poses a requirement on the maximum value of the smallest vertical wavenumber in ice. With the same reasoning as before, it results:

$$k_z^{small} < \frac{1}{a}\frac{2\pi}{\Delta H_{z,ice}^{min}}. \tag{11}$$

It is worth noting that at the typical incidence angles between $25\,^\circ$ and $60\,^\circ$ and for $\epsilon_{ice} = 3.2$, the factor a is larger than 1, leading to values of the required vertical wavenumbers in air smaller than the ones in ice. This could be of advantage depending on the specific realization of the multi-baseline measurements in a mission context. In fact, limit values of the perpendicular baselines are calculated from the limit values of the vertical wavenumbers in air. In the far field, the vertical wavenumber defined in Eq. (1) can be approximated as a function of the perpendicular baseline $B_\perp$ and of the slant range distance R as:

$$k_z \approx \frac{4\pi}{\lambda}\frac{B_\perp}{R\sin(\theta)} \Rightarrow B_\perp \approx k_z\frac{\lambda R\sin(\theta)}{4\pi}. \tag{12}$$

It is not straightforward to put requirements on the minimum number and configuration of the vertical wavenumbers providing a meaningful TomoSAR reconstruction in which two peaks are distinguishable at the physical interfaces. Therefore, we investigate this issue by reconstructing the vertical reflectivity profile of the total power by selecting low-dimensional wavenumber configurations from the real data set used in this study. The mean X-band polarimetric multi-baseline covariance matrix averaged over the central transect of Lake 3 is considered for this evaluation. For a 1-meter thick ice layer, the results of this study suggest that $\delta_{z,ice}^{max} = 1\,$m or better is required to separate both interfaces. On the other hand, to reconstruct an ambiguity-free reflectivity profile, a minimum $\Delta H_{z,ice}^{min} = 2\,$m in ice is recommended. For the selected data, the incidence angle is $42\,^\circ$, leading to $k_z^{large} > 4.4\,$rad/m and $k_z^{small} < 2.2\,$rad/m. The profile reconstructions for the selected configurations

https://doi.org/10.5194/egusphere-2026-5452
Preprint. Discussion started: 25 September 2026

are shown in Fig. 12 and Fig. 13, respectively. Configuration A corresponds to the entire set of passes, and is the configuration used in the rest of the study. In configuration B, the largest baseline has been omitted, leading to a coarser resolution in height. Indeed the associated reconstruction does not exhibit the two peaks. Configurations C and D have only four and three passes, yet they meet the criteria on the vertical wavenumbers. Both configurations lead to a profile of total power where the two peaks can be successfully detected.

A final point concerns how a possible spaceborne implementation could be envisioned, again for X-band SAR measurements. An implementation as in the SKaDI concept (Hajnsek et al., 2022) foresees bistatic interferometric measurements with an incidence angle of 30 ° and orbit height of 519 km. With this geometry, and again for $\delta_{z,ice}^{max} = 1$ m and $\Delta H_{z,ice}^{min} = 2$ m, it results $k_z^{large} > 3.9$ rad/m and $k_z^{small} < 1.95$ rad/m. The corresponding perpendicular baselines are larger than 5.7 km and smaller than 2.8 km, respectively. It is important to remember that, as stated in Sect. 2, the perpendicular baseline should not exceed the critical baseline to avoid complete decorrelation. The critical baseline is calculated in the bistatic case as (Gatelli et al., 1994):

$$B_{\perp,crit} = \frac{2WR\lambda\tan(\theta)}{c} \tag{13}$$

where W is the system bandwidth and c is velocity of light in vacuum. In the case above, the smallest and largest perpendicular baselines already correspond to the 40 % and the 80 % of the critical baseline assuming a chirp bandwidth of 100 MHz. Multiple bistatic acquisitions with varying perpendicular baselines are therefore required to obtain a sufficient number of non-decorrelating SLC pairs for a meaningful TomoSAR reconstruction. Minimum configurations such as the ones in Fig. 13 may not be sufficient. However, the revisit time between one acquisition and the next might become the main limitation: if too long, changes in the scenes may reduce the physical significance of the TomoSAR reconstruction. Changing bandwidth, acquisition geometry and/or opting for a multi-static implementation are all critical components. For instance, considering a dual-baseline MirrorSAR implementation (Krieger et al., 2018), with an incidence angle of 40 ° and an orbit height of 500 km, would result into $k_z^{large} > 4.3\,rad/m$. This is equivalent to a perpendicular baseline of 8.7 km, i.e., 52 % of the critical baseline, for a chirp bandwidth of 150 MHz. Increasing the number of acquisitions to counteract decorrelation in the TomoSAR reconstructions would then be a less critical requirement.

7 Conclusion

In this article, we explored the information content of X- and C-band polarimetric multi-baseline data over Arctic lake ice acquired during the PermASAR campaign by means of Pol-TomoSAR 3-D reconstructions of polarimetric covariance matrices. The chosen Pol-TomoSAR algorithm allowed to retrieve meaningful reconstructions despite the thinness of the ice layer. Based on field observations, peaks at different heights in the reconstructions could be attributed to the air/ice and ice/water interfaces at the boundaries of the lake ice layer. The main findings of the article are summarized below.

- Both X- and C-band showed strong contributions from the air/ice and ice/water interfaces, with a weaker air/ice interface at C-band. Some variability within the lakes and in between the lakes has been observed, backscattering contributions

https://doi.org/10.5194/egusphere-2026-5452
Preprint. Discussion started: 25 September 2026

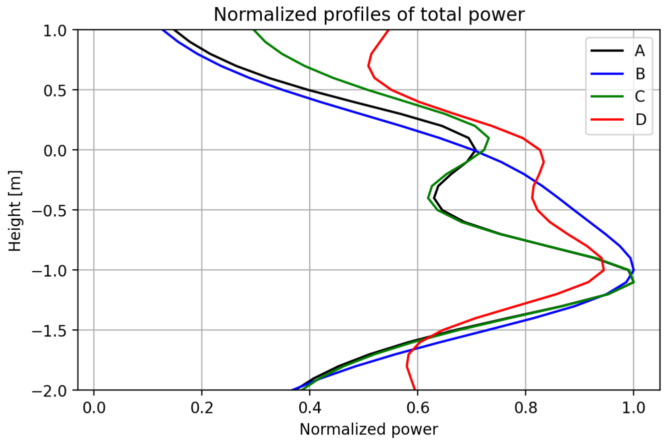

Figure 12. Reconstructed profiles from different baseline configurations (A, B, C, D). The wavenumber configurations and associated Rayleigh resolution limit and height of ambiguity are shown in Fig. 13.

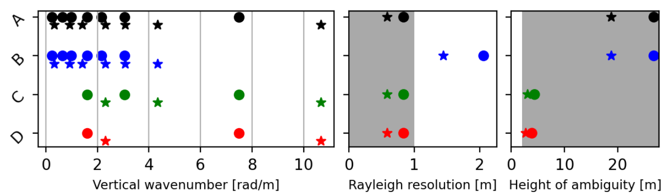

Figure 13. The left plot shows the distribution of the vertical wavenumbers selected for each configuration. Only the vertical wavenumbers calculated with respect to the first pass are shown. The middle and right plots show the Rayleigh resolution limit and the height of ambiguity associated with each configuration. The gray zones indicate the values for which a $\delta_{z,ice}^{max} = 1m$ and $\Delta H_{z,ice}^{min} = 2m$ are met. In all plots, dots indicate values in air while stars indicate values in ice.

within the ice volume have been observed as well. As a consequence, we suggest that the usual hypothesis that the radar signal, in particular at C-band, is coming solely from the ice/water interface, does not always hold. Therefore, care should be taken while deriving ice thickness characteristics under this hypothesis. The X-band signal was more consistently sensitive to both air/ice and ice/water interfaces, making it the most promising for modeling and inversion of the ice thickness.

– The polarimetric analysis at both air/ice and ice/water interfaces indicates mixed scattering that does not only consist in rough surface scattering. We hypothesized that at the upper interface and especially at X-band, the thin snow cover contributes to the backscatter. At the lower interface, there is a possible contribution from gas bubbles entailed in the congelation ice, that can lead to volume scattering or dihedral backscattering. Future work could include a model-based approach to disambiguate the scattering mechanisms at the ice/water interface, and a further airborne SAR campaign associated with extensive fieldwork to support the analysis.

https://doi.org/10.5194/egusphere-2026-5452
Preprint. Discussion started: 25 September 2026

- The C-band signal proved to be most sensitive to the presence of high-entropy regions. Several mechanisms were considered to explain the observed high-entropy signal. These regions were consistent with the presence of a layer of snow-ice above the congelation ice. As the Pol-TomoSAR techniques allowed to locate the scattering contributions in height, it was found that these regions were focused at the ice/water interface. This observation is inconsistent with the usual hypothesis of volume scattering from the possible snow-ice layer, but is consistent with a dihedral backscatter mechanism with the possible snow-ice layer and the ice/water interface.

- Reducing the number of baselines used in the tomographic reconstruction, we found that three acquisitions (dual-baseline) were sufficient to reconstruct a profile with two peaks at the ice layer boundaries. However, depending on the mission implementation, a larger number of acquisitions might be needed due to the required high vertical resolution, or equivalently, large perpendicular baselines. This is a critical limitation also for employing data acquired by (single-pass) interferometric missions like DLR's TanDEM-X. Definitely, there is potential for future spaceborne SAR missions with multi-static capabilities to estimate Arctic lake ice thickness with an appropriate choice of baselines. We believe that the results in this study can support their definition, and the design of appropriate inversion models and algorithms.

Appendix A: Appendix: reconstructed power profiles in the lexicographic basis

Analyzing reconstructed power profiles for several polarizations in the lexicographic basis is useful in order to allow the comparison with existing results based on backscatter and to support planning for future missions, as few spaceborne SAR systems have fully polarimetric capabilities. Reconstructed profiles in the lexicographic basis are shown for the study lakes, at X-band in Fig. A1 and at C-band in Fig. A2, on the same azimuth transects than in Sect. 4.1. Contrary to Sect. 4.1, the reconstructed profiles are normalized to their own maximum at each azimuth position in order to enhance the location of the main contribution for each polarization individually. Therefore, backscatter power variations are not preserved in between lakes or polarizations, nor along the transect. Polarization-specific observations can be made, that are valid for both X-band and C-band:

- At HH polarization, most lakes exhibit a strong contribution from the lower interface. Some lakes (Lake 3, Lake 4b) also show a contribution from the upper interface.

- at VV, there is some variability between lakes, as for some lakes the VV contribution is stronger at the upper interface (Lake 3, Lake 4b), for some it is stronger at the lower interface (Lake 1, Lake 2, Lake 4a), and for some there are contributions at both interfaces (Lake 5 at X-band).

- at HV, the main contribution can be attributed to the lower interface for all study lakes.

It is worth noting that even for a single polarization, the observed tomographic response from neighboring lakes is diverse.

https://doi.org/10.5194/egusphere-2026-5452
Preprint. Discussion started: 25 September 2026

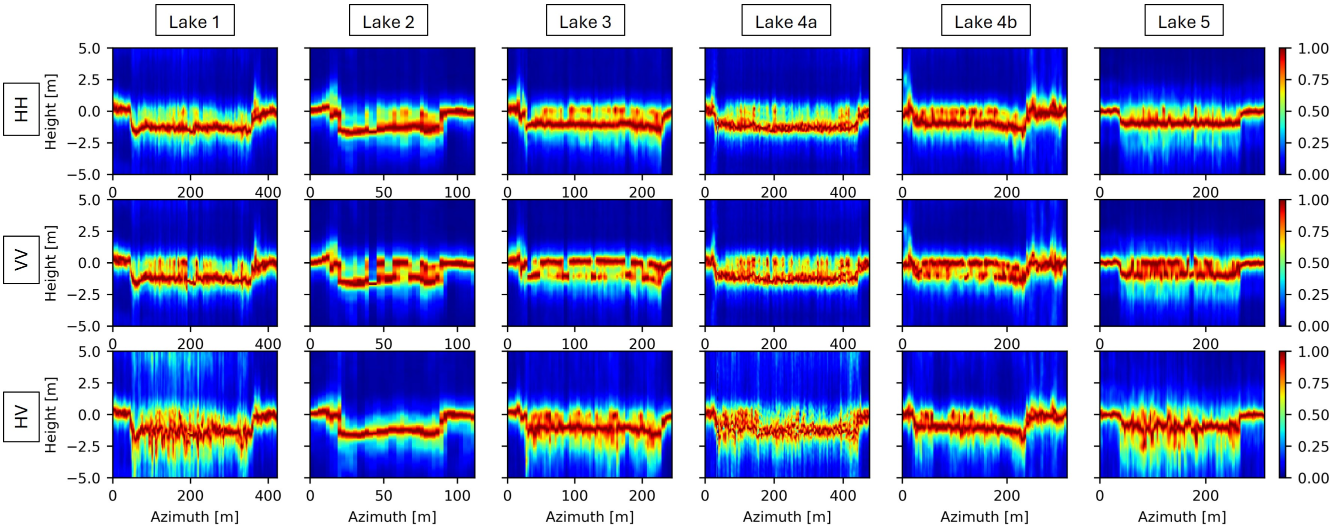

Figure A1. Capon Pol-TomoSAR power reconstructions along azimuth transects at the study lakes, X-band. The transects are in the lexicographic basis: the first row corresponds to HH, the second row to VV and the third row to HV. Each column corresponds to a different lake, from Lake 1 to Lake 5. Each profile is normalized to its own maximum at each azimuth bin.

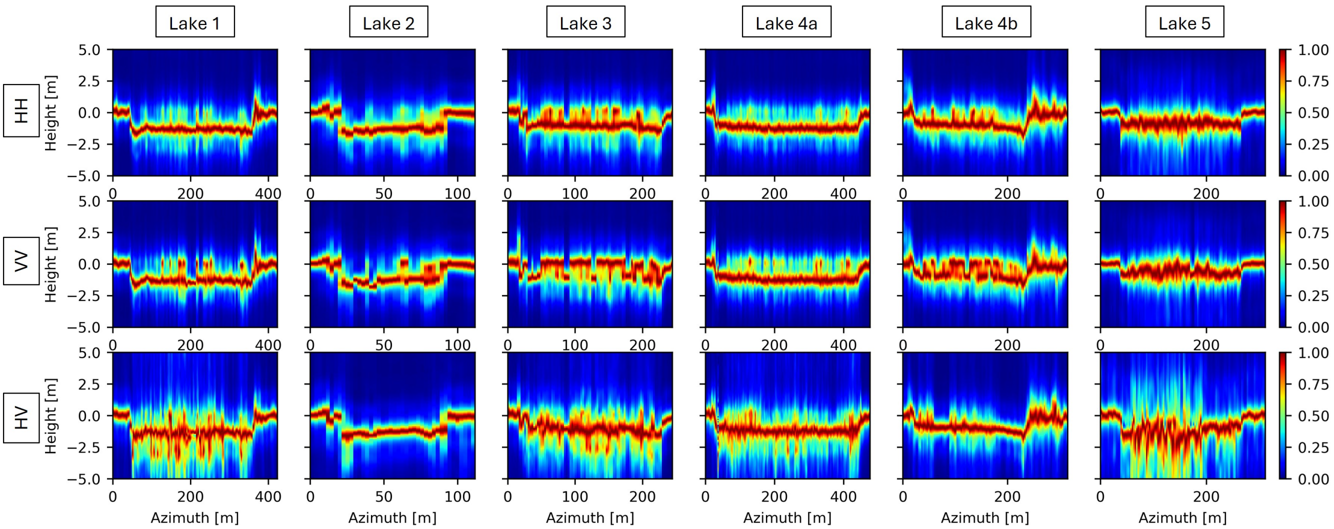

Figure A2. Capon Pol-TomoSAR power reconstructions along azimuth transects at the study lakes, C-band. The transects are in the lexicographic basis: the first row corresponds to HH, the second row to VV and the third row to HV. Each column corresponds to a different lake, from Lake 1 to Lake 5. Each profile is normalized to its own maximum at each azimuth bin.

Data availability. The SAR data set used in this study was acquired during an experimental airborne campaign and is currently being used as part of a PhD thesis. Therefore, this data set is not yet publicly available. The other data sets used in this study are publicly available and are cited accordingly in the manuscript.

https://doi.org/10.5194/egusphere-2026-5452
Preprint. Discussion started: 25 September 2026

Author contributions. PS and MP developed the methodology. PS performed the data analysis. MP provided expertise in SAR tomography. EW and JB provided expertise in hydrology of Arctic environments. PS prepared the manuscript with contributions from all co-authors. IH provided overall supervision and guided the content of the paper.

Competing interests. The authors declare that they have no conflict of interest.

Acknowledgements. This article was developed in the frame of a PhD thesis supported by the German Academic Exchange Service (DAAD). The authors would like to thank Natural Resources Canada for their collaboration during the PermASAR campaign conducted in 2018 and 2019. Further, we would like to thank the DLR F-SAR processing team for the acquisition and pre-processing of the PermASAR data set, in particular Marc Jäger. We are also grateful to J. J. van der Sanden for the fruitful discussions about potential scattering contributions. This work represents a contribution to the Cluster of Excellence "Climate, Climatic Change, and Society" (CLICCS).

https://doi.org/10.5194/egusphere-2026-5452
Preprint. Discussion started: 25 September 2026

References

Al-Kahachi, N.: Polarimetric SAR modelling of a two-layer structure: A case study based on subarctic lakes, Ph.D. thesis, Technische Universität München, Germany, 2014.

Atwood, D. K., Gunn, G. E., Roussi, C., Wu, J., Duguay, C., and Sarabandi, K.: Microwave Backscatter From Arctic Lake Ice and Polarimetric Implications, IEEE Transactions on Geoscience and Remote Sensing, 53, 5972–5982, https://doi.org/10.1109/tgrs.2015.2429917, 2015.

Cazcarra-Bes, V., Pardini, M., and Papathanassiou, K.: Definition of Tomographic SAR Configurations for Forest Structure Applications at L-Band, IEEE Geoscience and Remote Sensing Letters, 19, 1–5, https://doi.org/10.1109/lgrs.2020.3027439, 2022.

Cloude, S.: Polarisation: applications in remote sensing, Oxford University Press, ISBN 9780199569731, 2009.

Cloude, S. and Pottier, E.: An entropy based classification scheme for land applications of polarimetric SAR, IEEE Transactions on Geoscience and Remote Sensing, 35, 68–78, https://doi.org/10.1109/36.551935, 1997.

Dall, J.: InSAR Elevation Bias Caused by Penetration Into Uniform Volumes, IEEE Transactions on Geoscience and Remote Sensing, 45, 2319–2324, https://doi.org/10.1109/tgrs.2007.896613, 2007.

Ferro-Famil, L., Huang, Y., and Reigber, A.: High-Resolution SAR Tomography using full rank Polarimetric spectral estimators, in: IEEE International Geoscience and Remote Sensing Symposium, pp. 5194–5197, https://doi.org/10.1109/igarss.2012.6352439, 2012.

Gatelli, F., Monti Guarnieri, A., Parizzi, F., Pasquali, P., Prati, C., and Rocca, F.: The wavenumber shift in SAR interferometry, IEEE Transactions on Geoscience and Remote Sensing, 32, 855–865, https://doi.org/10.1109/36.298013, 1994.

Gow, A. J.: Orientation textures in ice sheets of quietly frozen lakes, Journal of Crystal Growth, 74, 247–258, https://doi.org/https://doi.org/10.1016/0022-0248(86)90114-4, 1986.

Gow, A. J. and Langston, D.: Growth history of lake ice in relation to its stratigraphic, crystalline and mechanical structure, US Army Cold Regions Research and Engineering Laboratory, CRREL Report 77–1, 1977.

Grünberg, I. and Boike, J.: Vegetation map of Trail Valley Creek, Northwest Territories, Canada, PANGAEA [data set], https://doi.org/10.1594/PANGAEA.904270, 2019.

Grünberg, I., Wilcox, E. J., Zwieback, S., Marsh, P., and Boike, J.: Linking tundra vegetation, snow, soil temperature, and permafrost, Biogeosciences, 17, 4261–4279, https://doi.org/10.5194/bg-17-4261-2020, 2020.

Gunn, G. E., Duguay, C. R., Atwood, D. K., King, J., and Toose, P.: Observing Scattering Mechanisms of Bubbled Freshwater Lake Ice Using Polarimetric RADARSAT-2 (C-Band) and UW-Scat (X- and Ku-Bands), IEEE Transactions on Geoscience and Remote Sensing, 56, 2887–2903, https://doi.org/10.1109/tgrs.2017.2786158, 2018.

Hajnsek, I., Pottier, E., and Cloude, S.: Inversion of surface parameters from polarimetric SAR, IEEE Transactions on Geoscience and Remote Sensing, 41, 727–744, https://doi.org/10.1109/tgrs.2003.810702, 2003.

Hajnsek, I., Aðalgeirsdóttir, G., Bartsch, A., Rodriguez Cassola, M., Fischer, G., Gierlich, R., Grosse, G., Haas, C., Huber, S., and Jesswein, K.: The Ka-band interferometric radar mission proposal for cold environments-SKADI, ESA Living Planet Symposium, 2022.

Hobbs, P. V.: Ice physics, Oxford University Press, ISBN 9780199587711, 2010.

Hoekman, D. and Vissers, M.: A new polarimetric classification approach evaluated for agricultural crops, IEEE Transactions on Geoscience and Remote Sensing, 41, 2881–2889, https://doi.org/10.1109/tgrs.2003.817795, 2003.

Jeffries, M. O., Morris, K., Weeks, W. F., and Wakabayashi, H.: Structural and stratigraphie features and ERS 1 synthetic aperture radar backscatter characteristics of ice growing on shallow lakes in NW Alaska, winter 1991–1992, Journal of Geophysical Research: Oceans, 99, 22 459–22 471, https://doi.org/10.1029/94jc01479, 1994.

https://doi.org/10.5194/egusphere-2026-5452
Preprint. Discussion started: 25 September 2026

Joerg, H., Pardini, M., Hajnsek, I., and Papathanassiou, K. P.: 3-D Scattering Characterization of Agricultural Crops at C-Band Using SAR Tomography, IEEE Transactions on Geoscience and Remote Sensing, 56, 3976–3989, https://doi.org/10.1109/tgrs.2018.2818440, 2018.

Krieger, G., Zonno, M., Mittermayer, J., Moreira, A., Huber, S., and Rodriguez-Cassola, M.: MirrorSAR: A Fractionated Space Transponder Concept for the Implementation of Low-Cost Multistatic SAR Missions, in: 12th European Conference on Synthetic Aperture Radar (EUSAR), pp. 1–6, VDE, 2018.

Michel, B. and Ramseier, R. O.: Classification of river and lake ice, Canadian Geotechnical Journal, 8, 36–45, https://doi.org/10.1139/t71-004, 1971.

Moreira, A., Prats-Iraola, P., Younis, M., Krieger, G., Hajnsek, I., and Papathanassiou, K. P.: A Tutorial on Synthetic Aperture Radar, IEEE Geoscience and Remote Sensing Magazine, 1, 6–43, https://doi.org/10.1109/mgrs.2013.2248301, 2013.

Morris, K., Jeffries, M. O., and Weeks, W. F.: Ice processes and growth history on Arctic and sub-Arctic lakes using ERS-1 SAR data, Polar Record, 31, 115–128, https://doi.org/10.1017/s0032247400013619, 1995.

Reigber, A. and Moreira, A.: First demonstration of airborne SAR tomography using multibaseline L-band data, IEEE Transactions on Geoscience and Remote Sensing, 38, 2142–2152, https://doi.org/10.1109/36.868873, 2000.

Reigber, A., Scheiber, R., Jager, M., Prats-Iraola, P., Hajnsek, I., Jagdhuber, T., Papathanassiou, K. P., Nannini, M., Aguilera, E., Baumgartner, S., Horn, R., Nottensteiner, A., and Moreira, A.: Very-High-Resolution Airborne Synthetic Aperture Radar Imaging: Signal Processing and Applications, Proceedings of the IEEE, 101, 759–783, https://doi.org/10.1109/jproc.2012.2220511, 2013.

Saporta, P., Alonso-González, A., Hammar, J., Grünberg, I., Boike, J., and Hajnsek, I.: Observing Seasonal Variabilities of a Permafrost Landscape With PolSAR, InSAR and Pol-InSAR, IEEE Journal of Selected Topics in Applied Earth Observations and Remote Sensing, 18, 10 733–10 748, https://doi.org/10.1109/jstars.2025.3551422, 2025.

Sauer, S., Ferro-Famil, L., Reigber, A., and Pottier, E.: Three-Dimensional Imaging and Scattering Mechanism Estimation Over Urban Scenes Using Dual-Baseline Polarimetric InSAR Observations at L-Band, IEEE Transactions on Geoscience and Remote Sensing, 49, 4616–4629, https://doi.org/10.1109/tgrs.2011.2147321, 2011.

Siles, G., Leconte, R., and Peters, D. L.: Retrieval of Lake Ice Characteristics from SAR Imagery, Canadian Journal of Remote Sensing, 48, 379–399, https://doi.org/10.1080/07038992.2022.2042227, 2022.

van der Sanden, J. J., Geldsetzer, T., Short, N., and Brisco, B.: Advanced SAR Applications for Canada's Cryosphere (Freshwater Ice and Permafrost) - Final Technical Report for the Government Related Initiatives Program (GRIP), 2012.

Vecchia, A., Pardini, M., Bruzzone, L., and Papathanassiou, K. P.: Improving Capon Polarimetric Tomographic SAR Reconstructions in Forest Scenarios, submitted to IEEE Geoscience and Remote Sensing Letters, 2026.

Wakabayashi, H., Motohashi, K., and Maezawa, N.: Monitoring Lake Ice in Northern Alaska with Backscattering and Interferometric Approaches Using Sentinel-1 Sar Data, in: IEEE International Geoscience and Remote Sensing Symposium, pp. 4202–4205, https://doi.org/10.1109/igarss.2019.8900371, 2019.

Weeks, W. F., Sellmann, P., and Campbell, W. J.: Interesting Features Of Radar Imagery Of Ice-Covered North Slope Lakes, Journal of Glaciology, 18, 129–136, https://doi.org/10.3189/s0022143000021572, 1977.

Weeks, W. F., Gow, A. J., and Schertler, R. J.: Ground-truth observations of ice-covered North Slope lakes imaged by radar, US Army Cold Regions Research and Engineering Laboratory, CRREL Report 81–19, 1981.

Wegmüller, U., Santoro, M., Werner, C., Strozzi, T., and Wiesmann, A.: Estimation of ice thickness of tundra lakes using ERS - ENVISAT cross-interferometry, in: IEEE International Geoscience and Remote Sensing Symposium, pp. 316–319, https://doi.org/10.1109/igarss.2010.5649026, 2010.

https://doi.org/10.5194/egusphere-2026-5452
Preprint. Discussion started: 25 September 2026

Wilcox, E. J.: Ice thickness, snow depth and lake properties for sampled lakes in and around the Trail Valley Creek watershed, NT, Borealis, V1 [data set], https://doi.org/10.5683/SP3/VP1UMC, 2025a.

Wilcox, E. J.: Lake bathymetry measurements for sampled lakes in and around the Trail Valley Creek watershed, NT, Borealis, V1 [data set], https://doi.org/10.5683/SP3/7XADY4, 2025b.

Wilcox, E. J., Wolfe, B. B., and Marsh, P.: Assessing the influence of lake and watershed attributes on snowmelt bypass at thermokarst lakes, Hydrology and Earth System Sciences, 26, 6185–6205, https://doi.org/10.5194/hess-26-6185-2022, 2022.

Wilcox, E. J., Wolfe, B. B., and Marsh, P.: Hydrological, meteorological, and watershed controls on the water balance of thermokarst lakes between Inuvik and Tuktoyaktuk, Northwest Territories, Canada, Hydrology and Earth System Sciences, 27, 2173–2188, https://doi.org/10.5194/hess-27-2173-2023, 2023.

Yitayew, T. G., Ferro-Famil, L., Eltoft, T., and Tebaldini, S.: Lake and Fjord Ice Imaging Using a Multifrequency Ground-Based Tomographic SAR System, IEEE Journal of Selected Topics in Applied Earth Observations and Remote Sensing, 10, 4457–4468, https://doi.org/10.1109/jstars.2017.2718998, 2017a.

Yitayew, T. G., Ferro-Famil, L., Eltoft, T., and Tebaldini, S.: Tomographic Imaging of Fjord Ice Using a Very High Resolution Ground-Based SAR System, IEEE Transactions on Geoscience and Remote Sensing, 55, 698–714, https://doi.org/10.1109/tgrs.2016.2613900, 2017b.

Zebker, H. and Villasenor, J.: Decorrelation in Interferometric Radar Echoes, IEEE Transactions on Geoscience and Remote Sensing, 30, 950–959, https://doi.org/10.1109/36.175330, 1992.